Supplementary Material for

# The impact of mapper experience and data on the quality of geomorphic fault mapping

Malinda G. Zuckerman[1,*], Chelsea P. Scott[1], J Ramon Arrowsmith[1], Rachel N. Adam[2], Chris Madugo[3], Rich D. Koehler[4], Albert Kottke[3], Hans AbramsonWard[5], Eldon Gath[6], Tania González[6], Brian Gray[5], Ozgur Kozaci[3], Thomas K. Rockwell[7], Trevor J. Austin[1], Tamarah King[8], Rachel Micander[4], Ethan Leuchter[5], Ian Pierce[3], Erin Alexander[1], Aube Gourdeau[9], Maximilien Laly[10], Izabelle Ogilvie[11], Sophie D. Rothman[12], Dominik R. Vlaha[4], Elaine K. Young[13], Veronica Prush[14], Christie Rowe[15], Madeline F.G. Schwarz[1].

[1]School of Earth and Space Exploration, Arizona State University, Tempe, Arizona 85287, USA
[2]Utah Geological Survey, Salt Lake City, Utah 84116, USA
[3]Geosciences Department, Pacific Gas and Electric Company, Oakland, California 94612, USA
[4]Nevada Bureau of Mines and Geology, University of Nevada, Reno, Nevada 89557, USA
[5]Lettis Consultants International, Inc., Concord, California 94520, USA
[6]Earth Consultants International, Inc., Santa Ana, California 92701, USA
[7]Department of Earth and Environmental Sciences, San Diego State University, San Diego, California 92182, USA
[8]Geoscience Australia, Symonston, Canberra, ACT 2609, Australia
[9] Département de physique, Collège de Maisonneuve, 3800 R. Sherbrooke E, Montréal, Québec H1X 2A2, Canada
[10]Faculty of Agricultural and Environmental Sciences, McGill University, Sainte-Anne-de-Bellevue, Québec H9X 3V9, Canada
[11]Environmental Systems Research Institute (Esri), Redlands, California 92373, USA
[12]Géosciences Environnement Toulouse, Toulouse, France
[13]California Geological Survey, Sacramento, California 95814, USA
[14]Department of Earth and Environmental Science, New Mexico Institute of Mining and Technology, Socorro, New Mexico 87801, USA
[15]Nevada Seismological Laboratory, University of Nevada, Reno, Nevada 89557, USA.
*Corresponding author: mgzucker@asu.edu, malindazuckerman@gmail.com

Contents of this file:

Text S1 to S3

Figures S1 to S6

Tables S1 to S7

Introduction

The Supplementary Material contains the following information:

*Section S1:* Readme for the GIS data file published in a Zenodo repository.

*Section S2:* Additional material on the methods.

*S2.1:* Prior knowledge for each mapper (Table S1).

*S2.2:* Data provided to mappers for each project: Repeat Mapping (Table S2), Data Type and Resolution (Table S3), and Adding a Geologic Map (Table S4).

*S2.3:* Graphical illustration of equations 1 and 2.

*S2.4:* Description for the *spatial spread of mapped faults near tectonic landforms* analysis.

*Section S3:* Additional results

*S3.1:* Statistics from the Repeat Mapping project. All Repeat Mapping statistics (Tables S5 & S6), Borah Peak statistics by principal and distributed ruptures (Table S7)

*S3.2:* Repeat Mapping results from the Northwest Ridgecrest and Southeast Ridgecrest mapping areas

*S3.3:* Results from the Data Type and Resolution project: Wasatch fault and Hope fault mapping areas

*S3.4:* Results from the Adding a Geologic Map project: West Napa fault

*Section S1:* Readme for the GIS data file published in a Zenodo repository.

The point geometry shape file (.shp) contains the following information:

This readme file was generated on 2022-08-17 by Mindy Zuckerman and updated on 2025-07-10

---

REPEATABILITY_SHAPEFILES

---

DATA & FILE OVERVIEW

Date of Data Collection: March 2022 – June 2022
Coordinate Reference System (CRS): EPSG:4326 – WGS 84

**File List**
We anticipate viewing our mapping point and linework on the open-source and free software QGIS (https://www.qgis.org). The shapefiles (.shp) will likely open in other GIS software such as Esri's ArcGIS, but the styles may look different than intended. Open the Repeatability.qgz file in QGIS to view all point and linework with symbology already loaded.

Included Files:

- **FCR folder:** Fault line shapefiles
- **Mapping_Polygons folder:** Line shapefiles of mapping area boundaries for each location
- **Repeatability QGIS project (.qgz):** Contains all shapefiles displayed with symbology. This project file must be opened with all files and folders in their original structure.

Files in the FCR Folders (for each mapping location):

- Shapefiles (.shp) for lines and polygon features
- QGIS Mapping Style files (.qml):
    - In the **FCR** folder, these style files set color and line thickness based on certainty ranking (e.g., strong to concealed) and primary vs. secondary faulting
- Definition files containing service properties, included to resolve potential data discrepancies

**Directory Structure for FCR Folders:**
**Level 1:** FCR folder
**Level 2:** Location folders
**Level 3:** Individual participant shapefiles

- Each location folder contains at least one style file associated with a participant's shapefile
- Styles can be copied to other shapefiles within QGIS
- With the correct folder structure, shapefiles with accompanying style files should automatically be symbolized correctly
- To apply a style manually, open the corresponding .qml file within the appropriate folder

**Definitions:**
**FCR:** Fault Confidence Ranking

Field Definitions:

- **Location:** Mapping area
  - BP = Borah Peak
  - EMC = El Mayor-Cucapah
  - FH = Fukushima-Hamadori
  - RC = Ridgecrest
- **Student:** Anonymized participant ID number
- **Level:** Experience level
  - Undergraduate
  - Graduate
  - Postdoc
  - Consultant1 (mid-career professional)
  - Consultant2 (senior professional)
- **Project_num:** Indicates whether this is the participant's 1st or 2nd mapping project
- **Fault_Exp:** Did the participant have prior knowledge of the fault? (yes/no)
- **Grade:** Map grade (not used)

*Section S2:* Additional material on the methods

*Section S2.1:* Prior knowledge of mapping and second project task for each participant

| ID | Level | Familiarity | Repeat Map | Second project |
|---|---|---|---|---|
| 1 | U | None | All | Other |
| 2 | U | None | All | Hope Fault data type/res. |
| 3 | U | None | All | Other |
| 4 | U | None | All | SSAF data type/res. |
| 5 | G | SSAF | All | Napa geologic map |
| 6 | G | None | All | Wasatch data type/res. |
| 7 | G | BP, RC, Napa, Southern California, NZ | No BP, RC | Wasatch data type/res. |
| 8 | G | None | All | EMC geologic map |
| 9 | G | None | All | Wasatch data type/res. |
| 10 | G | SSAF | All | EMC geologic map |
| 11 | G | None | All | Other |
| 12 | G | Napa, SSAF | All | Wasatch data type/res. |
| 13 | G | RC, Napa | All | Other |
| 14 | G | None | All | Other |
| 15 | G | None | All | EMC geologic map |
| 16 | P | RC | All | SSAF data type/res. |
| 17 | P | RC, Asia, SSAF, Idaho, SLC, NZ | All | Hope Fault data type/res. |
| 18 | MP | EMC, RC | All | N/A |
| 19 | MP | RC | All | N/A |
| 20 | MP | BP, EMC, RC | All | N/A |
| 21 | SP | BP | All | N/A |
| 22 | SP | BP, EMC, FH, RC | All | N/A |
| 23 | SP | None | All | N/A |

***Table S1.*** *Prior knowledge for each participant. Experience listed includes familiarity with the regions in which the mapping areas are located (i.e., New Zealand (Hope Fault), Napa (South Napa earthquake), Asia (Fukushima-Hamadori), Idaho (Borah Peak), and Southern California (Southern San Andreas Fault)) and the specific mapping areas. BP=Borah Peak, EMC=El Mayor-Cucapah, FH=Fukushima-Hamadori, NZ=New Zealand, RC=Ridgecrest, SLC=Salt Lake City (Wasatch Fault), SSAF=Southern San Andreas Fault.* U=undergraduate, G=graduate student, P=postdoctoral scholar, MP=mid-career professional geologist, SP=senior professional geologist. *Second projects listed as "other" include class projects not included in this study.*

Before mapping projects were assigned, mapping course participants reported if they had experience and/or familiarity with an area or region. We determined that participant #7 had too much experience with Borah Peak and Ridgecrest to complete those Repeat Mapping maps.

Professionals shared prior experience details after completing their maps. Participants declared familiarity with but no mapping experience of the coseismic ruptures in the areas. Participant #22 published geologic maps in the EMC area prior to the 2010 earthquake (Mueller & Rockwell, 1991, 1995). We did not use Borah Peak fault data from Mapper #21 due to technical difficulties.

*Section S2.2:* Data provided to mappers for each project: Repeat Mapping (Table S2), Data Type and Resolution (Table S3), and Adding a Geologic Map (Table S4).

| Earthquake | Cumulative geologic offset | Climate classification | Sense of slip | Data type; Resolution (m/pix) | Year data acquired |
|---|---|---|---|---|---|
| 1983 $M_w$ 6.9 Borah Peak | ~2 km | Cold semi-arid | Normal | DSM; 1.7 | 1952-1966 |
| 2010 $M_w$ 7.2 El Mayor-Cucapah | ~20 km | Hot desert | Normal, right-lateral strike-slip | DSM; 6 | 2006 |
| | | | | Satellite imagery; 1.2 | 2006 |
| 2011 $M_w$ 6.6 Fukushima-Hamadori | <10 km | Humid subtropical | Normal | DSM; 2 | 2006 |
| | | | | Satellite imagery; 1.3 | 2005 |
| 2019 $M_w$ 6.4 Ridgecrest | <1 km | Hot desert | Left-lateral strike-slip | DSM; 2 | 2007-2016 |
| | | | | Satellite imagery; 1 | 2017 |

***Table S2.*** *Repeat Mapping project earthquake background and data supplied to mappers. Cumulative geologic offset data from Crone et al., (1987) and Mapel et al., (1965) (Borah Peak); Mueller and Rockwell (1995) (EMC), Toda and Tsutsumi, (2013); Nissen et al., (2014) (Fukushima-Hamadori), Thompson Jobe et al., 2020 (Ridgecrest). Climate type from Köppen-Geiger climate classification (Peel et al., 2007). DTM = Digital terrain model, DSM = Digital surface model. Borah Peak DSM from Reitman & Briggs, 2024; El Mayor Cucapah DSM (OpenTopography, 2012) and imagery accessed from Google Earth, captured 29 January 2006; Fukushima DSM from Nissen et al., 2014; Ridgecrest DSM (OpenTopography, 2019) and imagery accessed from Google Earth, captured 1 July 2017.*

| Mapping Area | Data Type | Resolution | Year |
|---|---|---|---|
| Wasatch Fault Areas 1 & 2<br>Salt Lake City, Utah, USA | NASA SRTM DSM | 30 m/pix | 2000 |
| | NAPP Airphoto | 1 m/pix | 1997 |
| | Satellite imagery | 1 m/pix | 2019 |
| | Airborne lidar, DSM | 0.5 m/pix | 2013-2014 |
| Hope Fault<br>South Island of New Zealand | NASA SRTM DSM | 30 m/pix | 2000 |
| | Satellite imagery | 1 m/pix | 2006 |
| | Airborne lidar DTM | 0.5 m/pix | 2014 |
| Southern San Andreas Fault | NASA SRTM DSM | 30 m/pix | 2000 |

| | | | |
|---|---|---|---|
| Southern California, USA | NAPP Airphoto | 1 m/pix | 2002 |
| | Satellite imagery | 1 m/pix | 2022 |
| | Airborne lidar, DSM | 1 m/pix | 2005 |
| | Structure-from-Motion, DSM | 0.1 m/pix | 2020 |

***Table S3.*** *Data Type and Resolution information for each map area. Wasatch fault: Google Earth imagery captured 12 Oct 2019; lidar (OpenTopography, 2014). Hope fault: Google Earth imagery captured 13 Dec 2006; lidar (OpenTopography, 2016). San Andreas fault: Google Earth imagery captured 11 Jun 2022; lidar (Delong, 2017); Structure-from-Motion* (Bunds et al., 2021). *NASA Shuttle Radar Topography Mission (SRTM) digital surface models (Farr & Kobrick, 2000). National Aerial Photography Program (NAPP) photos from the Earth Resources Observation and Science Center and the USGS (2017).*

| Mapping Area | Data Type | Resolution | Year |
|---|---|---|---|
| 2010 $M_w$ 7.2 El Mayor-Cucapah earthquake (32.409, -115.573) | Airborne lidar, DSM | 6 m/pix | 2006 |
| | Satellite imagery | 1 m/pix | 2009 |
| | Geologic map | 1:10,000 | 1991 |
| 2014 $M_w$ 6.0 South Napa earthquake (38.313, -122.358) | Airborne lidar, DSM | 1 m/pix | 2003 |
| | Satellite imagery | 1 m/pix | 2011 |
| | Geologic map | 1:100,0000 | 2007 |

***Table S4.*** *Adding a Geologic Map Project dataset information. El Mayor-Cucapah: DSM (OpenTopography, 2012), Google Earth satellite imagery captured 29 January 2009, geologic map (Mueller & Rockwell, 1991). Napa: DSM (OpenTopography, 2010); Google Earth imagery collected 30 December 2011; Geologic map (Graymer et al., 2007).*

*Section 2.3.* Graphical illustration of equations 1 and 2

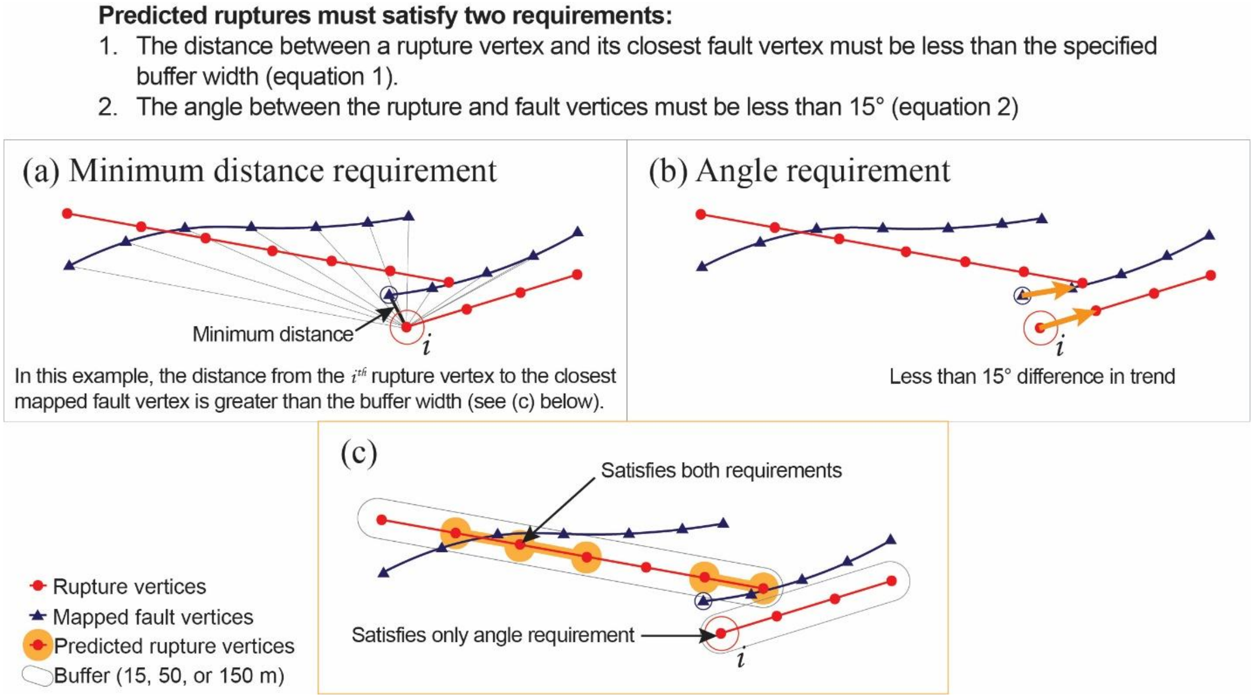


***Figure S1.*** *Graphical illustration of equations 1 and 2 for metric 1 (Section 2.5.3). A: For each rupture vertex, $i$ (red circles), we calculate the minimum separation distance from all, $n$ (blue triangles), fault vertices. The closest fault vertex must be within the specified buffer distance (A and C). B: The closest mapped fault, represented as a unit vector at each vertex, must trend within 15 degrees of the rupture vertex vector. C: For a rupture vertex to be defined as "predicted," the nearest fault vertex must be both within the specified buffer width AND within 15 degrees of the rupture vertex.*

*Section S2.4:* Description for the *spatial spread of mapped faults near tectonic landforms* method

This analysis (Section 3.2) considers how mappers with varying experience levels interpret fault location relative to tectonic landforms that are indicative of faulting. We examine the distribution of mapped pre-rupture fault locations along a profile perpendicular to the coseismic rupture (Figure 7) and centered on a geomorphic indicator point (GIR) mapped by multiple mappers (geomorphic indicator points are described in detail in Adam et al., 2025). Using all mappers' pre-rupture faults, we counted mapped faults within 1 m bins along profile lines oriented perpendicular to the rupture trend (Figure S1). We analyze the separation distance of mapped faults from coseismic ruptures partitioned by mapper experience level. Our analysis focuses on a fault scarp for the El Mayor-Cucapah and Northwest Ridgecrest areas and a triangular facet feature for the Fukushima-Hamadori area.

Using all mappers' pre-rupture faults, we calculate the spatial distribution of mapped pre-rupture faults along a profile. The profile is a one-meter-wide swath with equal divisions with which to count the faults parallel to the rupture. The calculation is made in MATLAB. As in Step 2 of the calculations in Section 2.6, we begin by converting coseismic ruptures and mapped faults to the local UTM zone, and then we resample to 1 m spacing. We specify the spacing and location of the profile; this includes a location along the rupture and the trend, length, and width of the divisions of the profile (Figure S1). We perform two-dimensional rotation to align the coordinate system to be perpendicular to the rupture locally at the GIR point of interest. We measure counts of the number of fault vertices within each swath division. The resulting counts can be used to display a bar graph of fault locations relative to the ruptures (Figure 7).

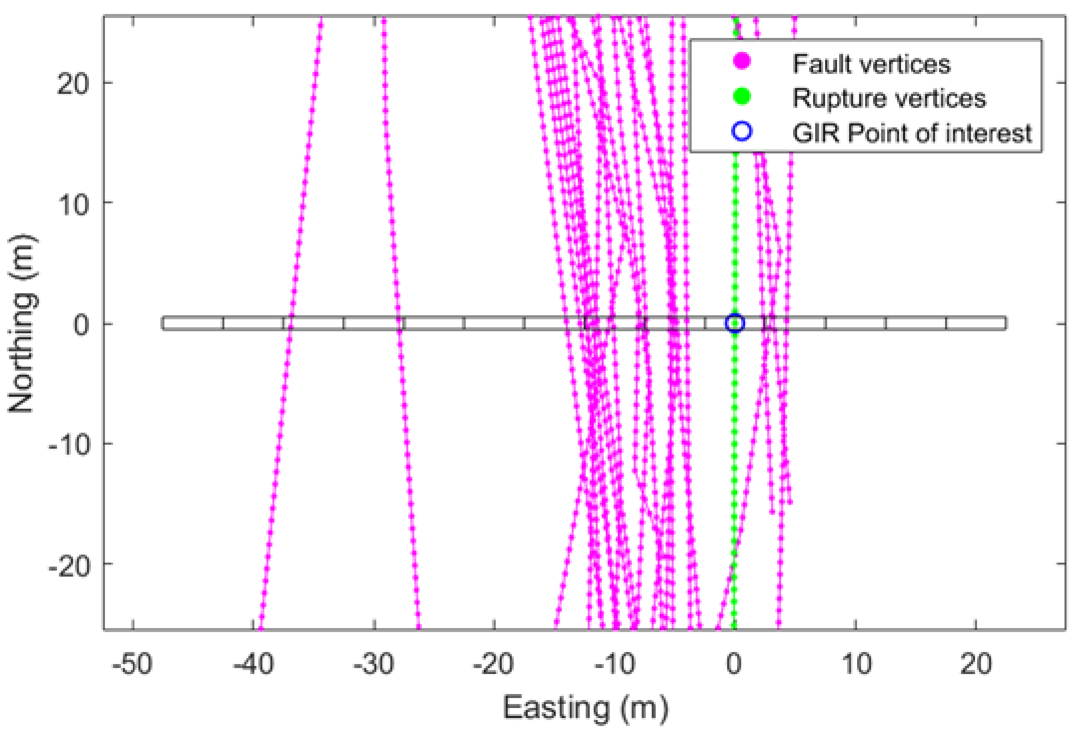


***Figure S2**. Visual demonstration of the spatial distribution of faults method. The profile spans across the El Mayor-Cucapah coseismic rupture vertices and their neighboring mapped fault vertices at the point of interest (Quaternary fault scarp, see Adam et al., 2025). Counts are* *measured inside each box of the swath and are then plotted in a bar graph (Figure 7, right column).*

*Section S3:* Additional results

*Section S3.1:* Statistics from the Repeat Mapping project

| Ruptures Predicted (%) | | | | | | | | | | |
|---|---|---|---|---|---|---|---|---|---|---|
| | **buffer** | **15 m** | | | **50 m** | | | **150 m** | | |
| | | **Median** | **Min** | **Max** | **Median** | **Min** | **Max** | **Median** | **Min** | **Max** |
| **BP** | **UG** | 1.5 | 0 | 3 | 7 | 0 | 22 | 18.5 | 4 | 35 |
| | **G (10)** | 1.5 | 0 | 7 | 13 | 4 | 33 | 33 | 8 | 51 |
| | **P** | 3 | 1 | 5 | 16.5 | 16 | 17 | 31.5 | 27 | 36 |
| | **C1** | 4 | 4 | 7 | 16 | 16 | 25 | 31 | 25 | 45 |
| | **C2 (2)** | 2.5 | 2 | 3 | 22.5 | 20 | 25 | 45.5 | 43 | 48 |
| **EMC** | **UG** | 16 | 14 | 18 | 48.5 | 27 | 56 | 64.5 | 33 | 65 |
| | **G** | 22 | 0 | 47 | 58 | 0 | 89 | 75 | 0 | 100 |
| | **P** | 31 | 26 | 36 | 70.5 | 55 | 86 | 87 | 74 | 100 |
| | **C1** | 25 | 19 | 35 | 70 | 61 | 87 | 100 | 100 | 100 |
| | **C2** | 33 | 19 | 37 | 83 | 78 | 89 | 100 | 100 | 100 |
| **FH** | **UG** | 17 | 1 | 60 | 52 | 43 | 81 | 92.5 | 73 | 97 |
| | **G** | 17 | 7 | 45 | 50 | 33 | 100 | 96 | 51 | 100 |
| | **P** | 18 | 15 | 21 | 57 | 47 | 67 | 94.5 | 89 | 100 |
| | **C1** | 18 | 18 | 30 | 71 | 68 | 89 | 100 | 97 | 100 |
| | **C2** | 20 | 18 | 21 | 49 | 36 | 53 | 97 | 84 | 100 |
| **RCNW** | **UG** | 8 | 0 | 27 | 25.5 | 0 | 68 | 39.5 | 0 | 77 |
| | **G (10)** | 29 | 16 | 36 | 57.5 | 38 | 64 | 67 | 46 | 86 |
| | **P** | 17 | 0 | 34 | 28 | 1 | 55 | 34.5 | 1 | 68 |
| | **C1** | 17 | 14 | 17 | 32 | 30 | 34 | 53 | 49 | 56 |
| | **C2** | 22 | 21 | 41 | 49 | 30 | 65 | 58 | 31 | 75 |
| **RCSE** | **UG** | 0 | 0 | 2 | 0 | 0 | 3 | 0 | 0 | 7 |
| | **G (10)** | 1.5 | 0 | 10 | 3 | 0 | 37 | 24.5 | 0 | 61 |
| | **P** | 0 | 0 | 0 | 0 | 0 | 0 | 2 | 0 | 4 |
| | **C1** | 0 | 0 | 0 | 0 | 0 | 5 | 0 | 0 | 31 |
| | **C2** | 0 | 0 | 0 | 0 | 0 | 3 | 0 | 0 | 14 |
| **All** | **UG** | 4.5 | 0 | 60 | 24.5 | 0 | 81 | 36.5 | 0 | 97 |
| | **G** | 10 | 0 | 47 | 45 | 0 | 89 | 67 | 0 | 100 |
| | **P** | 10 | 0 | 36 | 32 | 0 | 86 | 52 | 0 | 100 |
| | **C1** | 17 | 0 | 35 | 32 | 0 | 89 | 53 | 0 | 100 |
| | **C2** | 19.5 | 0 | 41 | 42.5 | 0 | 89 | 66.5 | 0 | 100 |

***Table S5.*** *Median, minimum, and maximum percentage of ruptures predicted by 15, 50, and 150 m buffer widths by mapping area and experience level. UG=undergraduate student (4),* *G=graduate student (11, unless otherwise stated), P=postdoctoral scholar (2), C1=mid-career professional geologist (3), C2=senior professional geologist (3, unless otherwise stated). BP=Borah Peak, EMC=El Mayor-Cucapah, FH=Fukushima-Hamadori, RCNW=northwest Ridgecrest area, RCSE=southeast Ridgecrest area.*

| Faults Ruptured (%) | | | | | | | | | | |
|---|---|---|---|---|---|---|---|---|---|---|
| | buffer | 15 m | | | 50 m | | | 150 m | | |
| | | Median | Min | Max | Median | Min | Max | Median | Min | Max |
| BP | UG | 1.5 | 0 | 3 | 6.5 | 0 | 15 | 22.5 | 3 | 31 |
| | G (10) | 2 | 0 | 7 | 13 | 3 | 33 | 30.5 | 9 | 47 |
| | P | 9 | 1 | 17 | 40.5 | 16 | 65 | 67 | 37 | 97 |
| | C1 | 6 | 5 | 9 | 27 | 16 | 32 | 46 | 28 | 50 |
| | C2 (2) | 3.5 | 3 | 4 | 25.5 | 21 | 30 | 45.5 | 37 | 54 |
| EMC | UG | 7 | 5 | 9 | 16 | 14 | 21 | 19.5 | 17 | 22 |
| | G | 7 | 0 | 13 | 18 | 0 | 25 | 22 | 0 | 32 |
| | P | 18 | 14 | 22 | 38.5 | 30 | 47 | 44.5 | 34 | 55 |
| | C1 | 4 | 3 | 14 | 10 | 9 | 31 | 24 | 17 | 34 |
| | C2 | 12 | 12 | 20 | 41 | 29 | 49 | 50 | 32 | 62 |
| FH | UG | 7 | 0 | 61 | 23 | 12 | 80 | 45.5 | 22 | 100 |
| | G | 6 | 1 | 13 | 24 | 5 | 37 | 43 | 16 | 57 |
| | P | 12 | 8 | 16 | 34 | 30 | 38 | 61.5 | 50 | 73 |
| | C1 | 6 | 5 | 10 | 29 | 21 | 31 | 46 | 43 | 49 |
| | C2 | 10 | 8 | 23 | 27 | 18 | 35 | 54 | 44 | 63 |
| RCNW | UG | 18.5 | 0 | 23 | 36 | 0 | 56 | 51.5 | 0 | 80 |
| | G (10) | 31.5 | 17 | 48 | 49.5 | 32 | 65 | 65 | 37 | 87 |
| | P | 29.5 | 0 | 59 | 58.5 | 31 | 86 | 71.5 | 52 | 91 |
| | C1 | 22 | 21 | 60 | 40 | 35 | 94 | 58 | 52 | 99 |
| | C2 | 34 | 34 | 48 | 62 | 40 | 74 | 83 | 54 | 87 |
| RCSE | UG | 0 | 0 | 1 | 0 | 0 | 1 | 0 | 0 | 8 |
| | G (10) | 0.5 | 0 | 5 | 1.5 | 0 | 34 | 9.5 | 0 | 88 |
| | P | 0 | 0 | 0 | 0 | 0 | 0 | 2 | 0 | 4 |
| | C1 | 0 | 0 | 0 | 0 | 0 | 7 | 8 | 0 | 38 |
| | C2 | 0 | 0 | 0 | 0 | 0 | 5 | 0 | 0 | 15 |
| All | UG | 3.5 | 0 | 61 | 14.5 | 0 | 80 | 21.5 | 0 | 100 |
| | G | 5 | 0 | 48 | 19.5 | 0 | 65 | 31.5 | 0 | 88 |
| | P | 11 | 0 | 59 | 30.5 | 0 | 86 | 51 | 0 | 97 |
| | C1 | 6 | 0 | 60 | 27 | 0 | 94 | 43 | 0 | 99 |
| | C2 | 11 | 0 | 48 | 29.5 | 0 | 74 | 52 | 0 | 87 |

**Table S6 (previous page).** Median, minimum, and maximum percentage of faults ruptured by 15, 50, and 150 m buffer widths by mapping area and experience level. UG=undergraduate student (4), G=graduate student (11, unless otherwise stated), P=postdoctoral scholar (2), C1=mid-career professional geologist (3), C2=senior professional geologist (3, unless otherwise stated). BP=Borah Peak, EMC=El Mayor-Cucapah, FH=Fukushima-Hamadori, RCNW=northwest Ridgecrest area, RCSE=southeast Ridgecrest area.

| buffer | 15 m | | | 50 m | | | 150 m | | |
|---|---|---|---|---|---|---|---|---|---|
| **PRINCIPAL** | | | | | | | | | |
| | med | min | max | med | min | max | med | min | max |
| U | 3 | 0 | 7 | 10 | 0 | 29 | 22 | 0 | 44 |
| G | 3 | 0 | 11 | 23 | 6 | 51 | 51 | 13 | 81 |
| P | 6 | 2 | 11 | 27 | 20 | 34 | 41 | 30 | 51 |
| MP | 8 | 7 | 12 | 29 | 26 | 40 | 60 | 41 | 74 |
| SP | 3 | 0 | 5 | 32 | 28 | 37 | 65 | 58 | 72 |
| **DISTRIBUTED** | | | | | | | | | |
| U | 0 | 0 | 1 | 3 | 0 | 15 | 15 | 8 | 27 |
| G | 0 | 0 | 4 | 5 | 0 | 16 | 17 | 3 | 36 |
| P | 0 | 0 | 0 | 7 | 1 | 13 | 24 | 5 | 43 |
| MP | 0 | 0 | 2 | 7 | 4 | 12 | 11 | 5 | 20 |
| SP | 2 | 1 | 3 | 14 | 5 | 23 | 29 | 18 | 40 |

**Table S7.** Median, minimum, and maximum percentage of principal and distributed 1983 Borah Peak earthquake ruptures predicted by experience level and buffer size. U=undergraduate, G=graduate student, P=postdoctoral scholar, MP=mid-career professional geologist, SP=senior professional geologist.

*Section S3.2:* Repeat Mapping results: Northwest Ridgecrest and Southeast Ridgecrest mapping areas

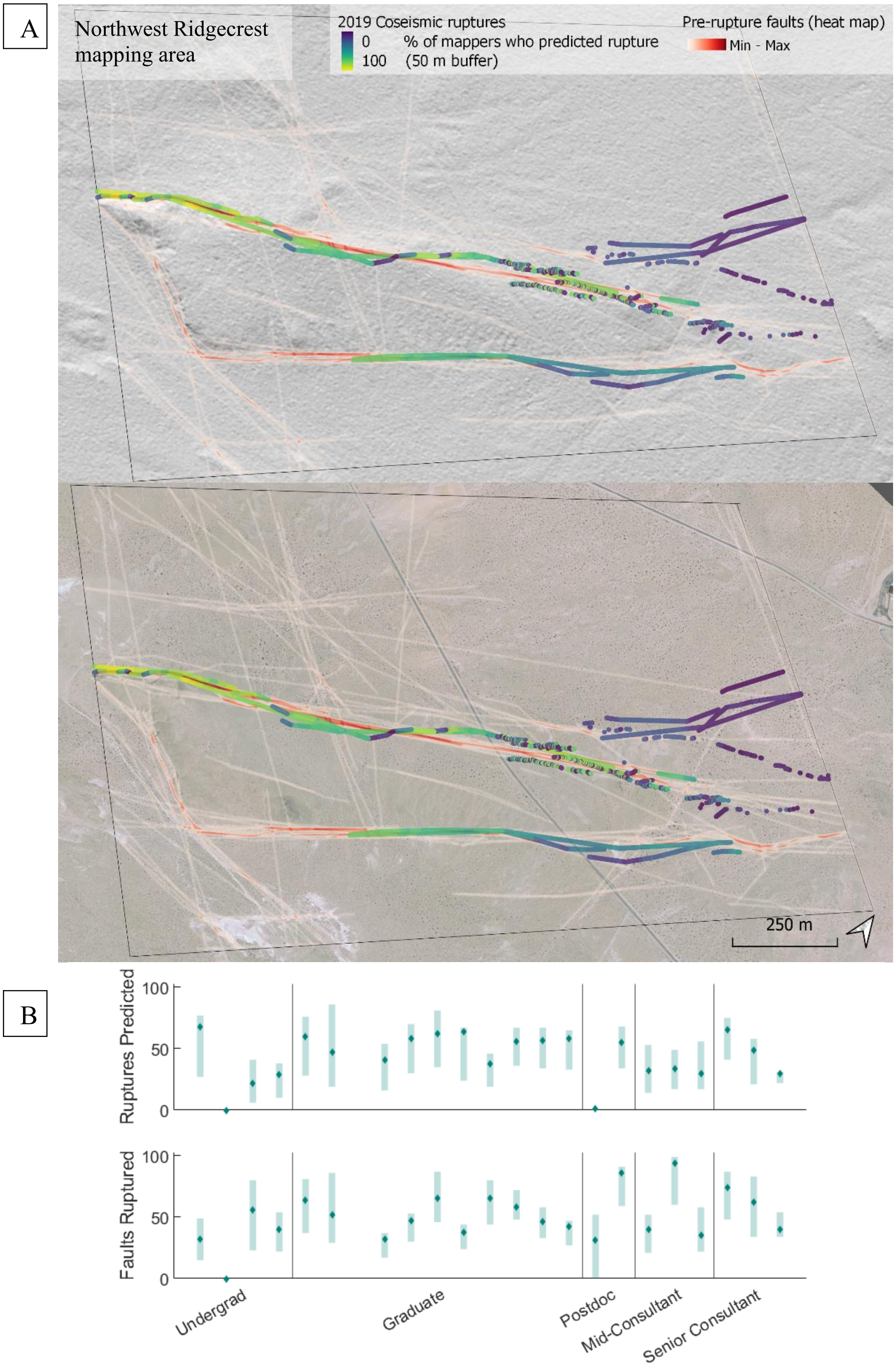

***Figure S3 (previous page).*** *(A) 2019* $M_w$ *6.4 Ridgecrest earthquake, northwest mapping area (centered at approximately 35.68°N, 117.54°W) with a heatmap of mapped faults and coseismic ruptures (DuRoss et al., 2020; Ponti et al., 2020; Sarmiento et al., 2021), colored by percentage of mappers who predicted the ruptures using a 50 m buffer, and mapped pre-rupture faults with pre-earthquake DSM hillshade (top) and satellite imagery (bottom). Basemaps are from OpenTopography, 2019 and Google Earth, 1 July 2017, Landsat/Copernicus. (B) Percentage of ruptures (top) and faults (bottom) for different buffer zones by mapper, divided by experience level. Diamond represents 50 m buffer, bottom of bar is for a 15 m buffer, and the top of the bar is for a 150 m buffer.*

The 2019 Mw 6.4 Ridgecrest earthquake ruptured 9.5 kilometers of southwest-trending left-lateral strike-slip fault in the Mojave Desert, California (Brandenberg et al., 2019; Ross et al., 2019). A Mw 7.1 earthquake, outside of our study area, occurred as a conjugate to the Mw 6.4 ruptures the next day. The landscape and surficial geology consist of broad alluvial cover, bedrock outcrops, ephemeral streams, and light-colored playa deposits. In the northwest mapping area, topographic relief is largely from a 1500 m-long bedrock ridge.

Mapped GIR features in the northwest mapping area include vegetation lineaments, cross-cutting relationships, and Quaternary fault scarps. All but two participants predicted ruptures along the pressure ridge. Most participants did not predict ruptures away from the ridge where there were few geomorphic markers (colored purple; Figure S2A). Faults mapped by postdocs and consultants generally trend in the same direction as the ruptures, but the faults mapped by undergraduate and graduate students do not.

Graduate students predicted the most ruptures (Figure S2B). There is only a small difference between the percentage of ruptures predicted versus faults that ruptured for individuals compared to other mapping areas. Participants mapped fewer faults that did not rupture, perhaps because the ruptures occurred around the singular topographic feature.

A

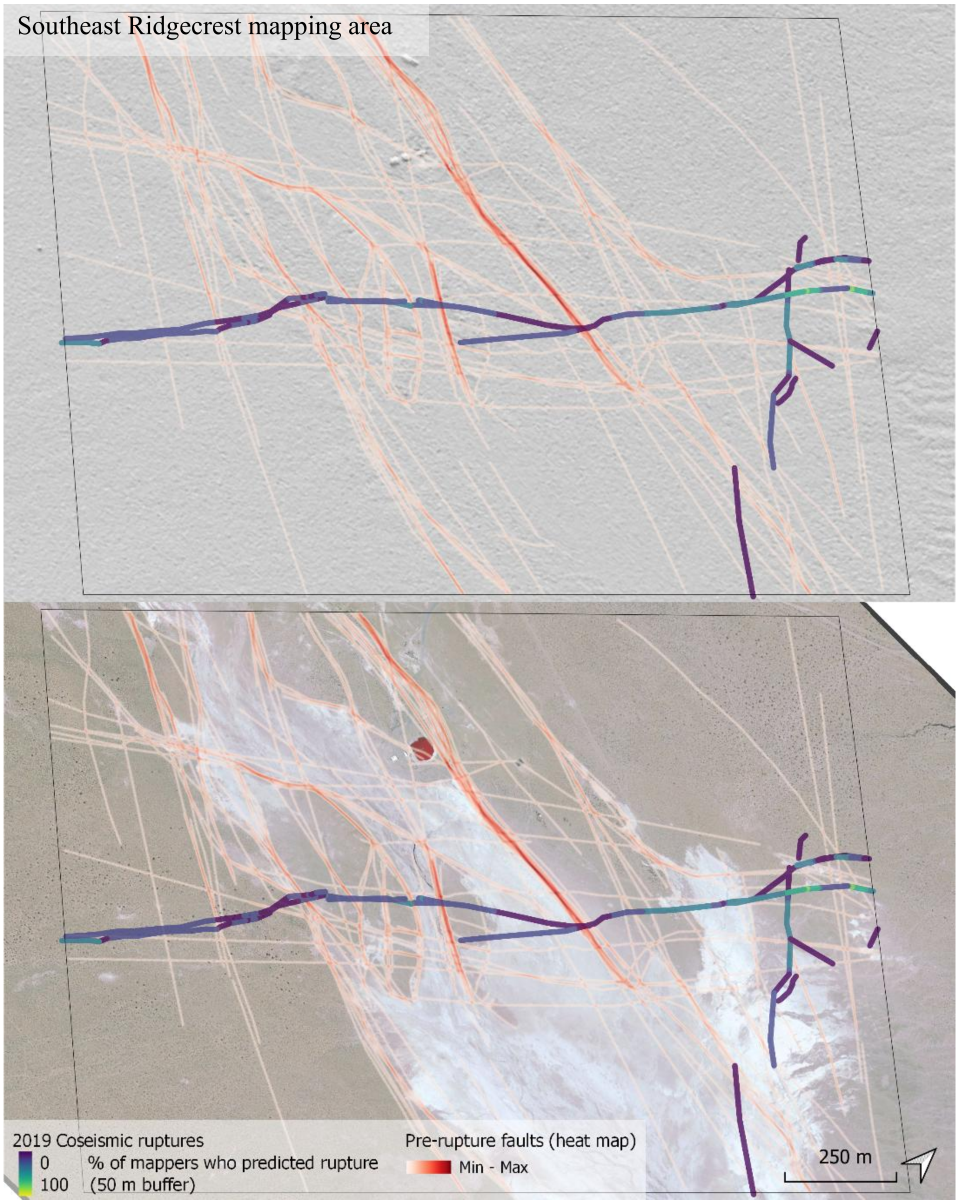
Southeast Ridgecrest mapping area
2019 Coseismic ruptures
0
100
% of mappers who predicted rupture
(50 m buffer)
Pre-rupture faults (heat map)
Min - Max
250 m

B

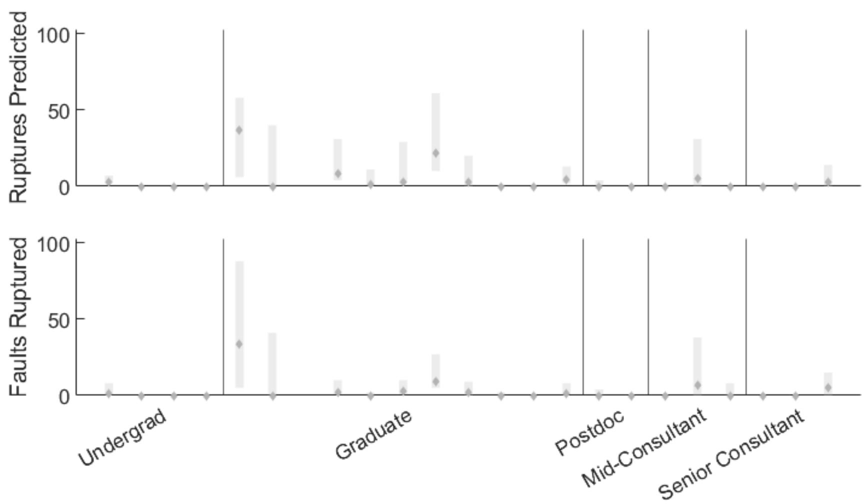
Ruptures Predicted
Faults Ruptured
100
50
0
Undergrad
Graduate
Postdoc
Mid-Consultant
Senior Consultant

***Figure S4 (previous page).*** *(A) 2019* $M_w$ *6.4 Ridgecrest earthquake, southeast mapping area (centered at approximately 35.66°N, 117.52°W) with a heatmap of mapped faults and coseismic ruptures (Sarmiento et al., 2021; DuRoss et al., 2020; Ponti et al., 2020), colored by percentage of mappers who predicted the ruptures using a 50 m buffer, and mapped pre-rupture faults atop pre-earthquake stereo imagery-derived DSM hillshade (top) and satellite imagery (bottom; OpenTopography.org, 2019; Google Earth, 1 July 2017, Landsat/Copernicus). (B) Percentage of ruptures (top) and faults (bottom) inside the buffer zones for each mapper. Diamond represents 50 m buffer, bottom of bar is for a 15 m buffer, and the top of the bar is for a 150 m buffer. Mappers are divided by experience level.*

The southeast Ridgecrest mapping area is 1.3 km from and has less relief than the northwest area. A fan-shaped playa deposit covers approximately a third of the mapping area and is most visible in the satellite imagery. The 2019 ruptures strike east-northeast and cut the playa deposits. The limited evidence of prior faulting includes a linear ridge and some tonal lineaments and contrast (Philibosian et al., 2020; Thompson Jobe et al., 2020).

The few mapped pre-rupture faults follow the trend of the coseismic ruptures (Figure S3A). One participant placed a fault within 50 m of a rupture for a 200 m along-strike distance, the most significant accurate prediction of ruptures of all participants. Participants placed faults based on tonal lineaments in the playa deposits that do not appear to reflect faulting.

Mapping outcomes did not improve with experience level (Figure S3B). The subtle topography in this area challenged the mappers. A few participants stated that they only mapped faults because they were instructed to.

*Section S3.3:* Data type and resolution project results: Wasatch Fault and Hope Fault

*Wasatch Fault, Salt Lake City, Utah*

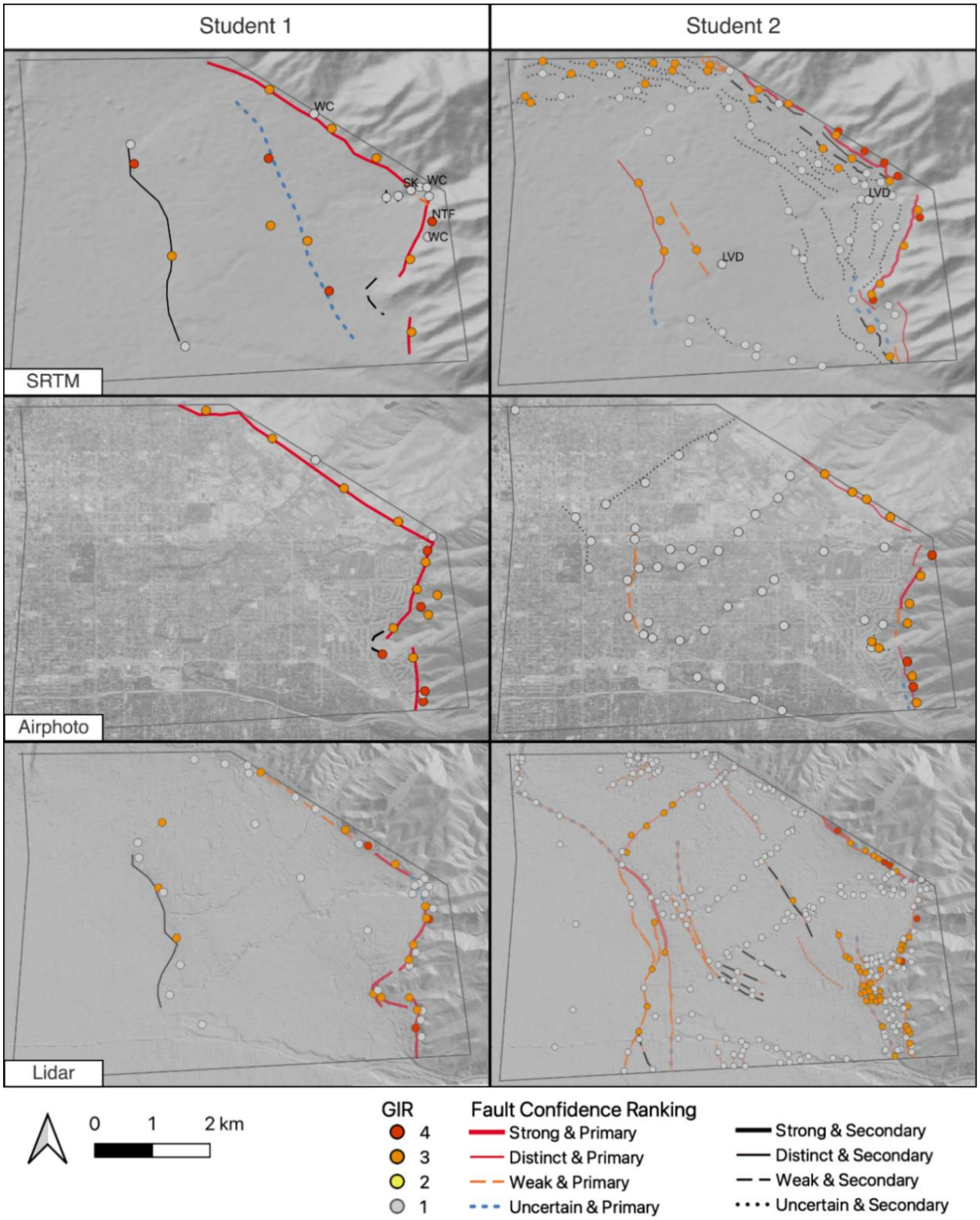


***Figure S5.*** *Participant maps of the Wasatch fault 2 location (centered at ~40.74°N, 111.84°W) on three different data type basemaps, Shuttle Radar Topography Mission 30 m DEM (top), National Aerial Photography Program airphoto (middle) and 1 m airborne lidar (bottom). Geomorphic indicator ranking points and fault line segments overlay hillshades (top and bottom) and aerial photo (middle). Point and line work were created by two graduate students. Datasets cited in Table S3.*

This mapping area is located in Salt Lake City, Utah, along the Wasatch fault. The climate is a semi-arid continental climate, and there are paleolake shorelines from the late Pleistocene Lake Bonneville (Benson et al., 1990). There is significant recent urban development along the Wasatch fault.

As shown in Figure S5, two graduate students completed geomorphic indicator point and fault mapping in the Wasatch Fault area. The students' maps differed, reflecting the influence of data interpretation, scale, and the lack of experience. Student 1 completed this as their first major assignment and mistakenly began with the airphoto rather than the intended 30 m SRTM hillshade.

The 30 m/pixel Shuttle Radar Topography Mission hillshade displays the range front and the valley, but not the built environment. Participants identified the Quaternary scarp in the valley (farthest west), but Student 1 mapped the scarp as secondary and Student 2 as primary. They both identified a fault along the base of the range front, citing triangular facet and over-steepened range front landforms (Machette et al., 1991). Student 1 mapped wineglass canyons between triangular facets. Both students mapped faults between the two main faults with low confidence. One southwest-trending drainage is visible in the middle of the mapping area. Student 1 mapped knickpoints where the drainage descends into the basin, and Student 2 added two linear valley/drainage GIR features along its length. Student 2 mapped landforms and faults with finer detail. In the northwest corner, Student 2 mapped less continuous and low-confidence faults and stated the challenges of determining if the faults were real from the 30 m DEM.

When using the airphoto, both participants reported reduced visibility of tectonic landforms due to the lack of elevation data and overprinting by anthropogenic features. Despite higher resolution, the airphoto led to fewer mapped faults. Student 1 omitted the main valley fault, possibly due to viewing this dataset first. Student 2 used vegetation and drainage patterns to infer fault locations but mapped more low-confidence traces, citing difficulty distinguishing shoreline features from fault scarps. In summary, mapping at a higher resolution is possible with the airphoto, but participants found that locating faults was more difficult than with lower resolution topography.

Even among similarly trained mappers, experience, data type, and sequence of interpretation affect fault mapping outcomes. Higher resolution alone does not guarantee better mapping; rather, map quality depends on how data are interpreted in context.

*Hope Fault, New Zealand*

This mapping area, on New Zealand's South Island, focuses on a 12 km section of the Hope fault that did not rupture in the 2016 Kaikoura earthquake. The ~2.5 cm/yr strike-slip Hope fault is located in a temperate oceanic climate (Manighetti et al., 2015; Peel et al., 2007). The results were not accompanied by a written report and the second mapper assigned to this location submitted a very short report and no geomorphic indicator mapping. So, this analysis is largely based on the fault linework.

The map based on the SRTM DEM contains a primary fault over the length of the map as well as a pressure ridge, shutter ridge, surface unit offset, bedrock scarp, and linear valley/drainage strike-slip features (not shown). Except for the bedrock scarp, these are all mid- to low-ranking features, yet the participant mapped most of the fault as strong confidence. Because of the coarse resolution of the DEM, geomorphic features along the fault are ambiguous, but the participant mapping is plausible.

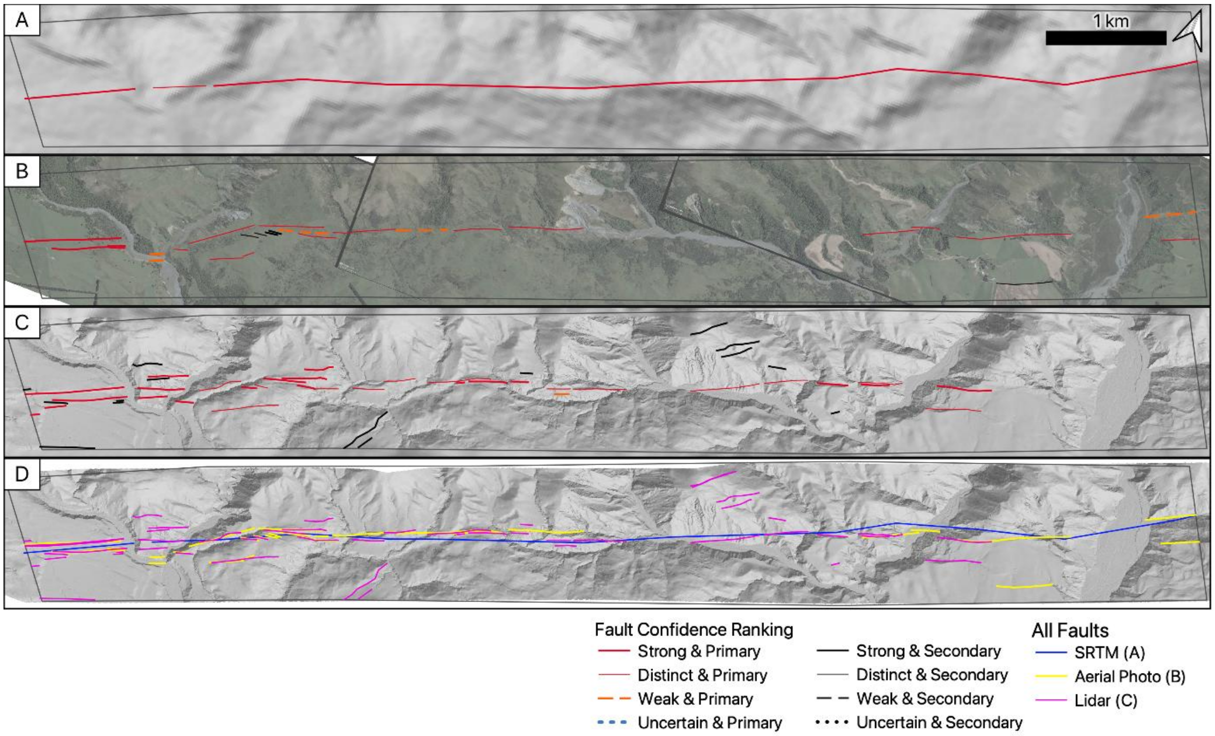


***Figure S6.*** *Participant fault map of the Hope Fault, New Zealand, South Island (centered at ~42.45°S, 173.23°E). Faults mapped based on Shuttle Radar Topography Mission DEM (A), Google Earth imagery (B), and airborne lidar (C). All faults are included in panel D to demonstrate differences in fault location and density. Faults mapped by a postdoctoral scholar. Refer to other figures for fault confidence ranking explanation. Datasets cited in Table S3.*

As shown in Figure S5B, the participant mapped nearly twice as many faults across a broader area using the satellite imagery relative to the 30 m DEM. With the satellite imagery, the participant mapped three primary faults with high confidence as well as a few secondary faults. Noticeably, the participant did not map faults where the geomorphology is dominated by active water, leaving a 2.5 km gap in the mapping area. The participant mapped faults consistent with the geomorphology. The participant did not map areas with high vegetation and fluvial activity, nor low-confidence faults.

The most notable change between satellite imagery and lidar mapping is the increased fault confidence. The participant mapped a 200 m-long weak-confidence fault and the rest with distinct or strong confidence. The participant mapped faults across the active water but did not map faults at the map's southeast corner. The participant mapped correct tectonic landforms, but could have mapped faults at a higher scale, considering the quality of the data. Specifically, continuous faults in the map center are straighter than the morphology suggests, and likely the participant did not zoom in enough to map with precision.

*Section S3.4:* Results from the fault mapping using a published geologic map project: West Napa fault

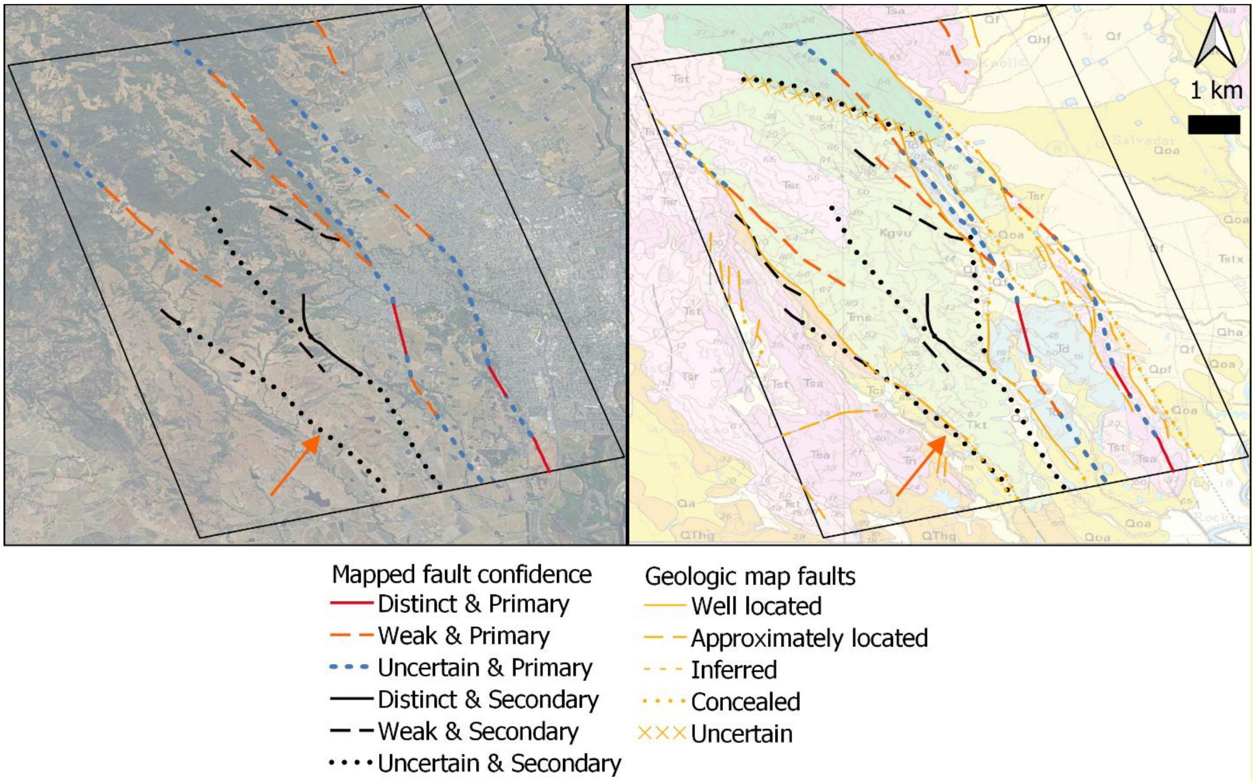


***Figure S7.*** *Participant mapped faults in South Napa Valley on pre-rupture Google satellite imagery basemaps (left) and then made revisions using a geologic map (right; Graymer et al., 2007). The orange arrow is referenced in the text; it points to the only instance of a fault segment location change after reviewing the geologic map. Maps created by a graduate student. Basemaps cited in Table S4.*

The Napa, CA mapping area, north of the San Francisco Bay, has a Mediterranean climate with wet winters and dry summers. Faults trend northwest-southeast along the range front (Graymer et al., 2007). The geology is obscured in the satellite imagery because of the vegetation and built environment (Figure S7). The area includes a portion of the 2014 South Napa earthquake.

As shown in Figure S7, the participant made few changes to the faults after reviewing the geologic map. The participant relocated one fault to better align with the faults mapped in the geologic map (orange arrow, Figure S7). There are vineyards and small drainages that cross the hillslope. The participant added a sag pond after reviewing the geologic map, but it is unclear if the depression is from a fault or agriculture. The participant removed only one initial fault segment and did not adjust certainty rankings after seeing the geologic map, even though the initial faults and faults on the geologic map are similar. The most significant change made was adding four fault segments. Two of these segments are at geologic contacts visible in the geologic map but not in the satellite. The participant did not add every fault in the geologic map.

**References**

Benson, L. V., Currey, D. R., Dorn, R. I., Lajoie, K. R., Oviatt, C. G., Robinson, S. W., Smith, G. I., & Stine, S. (1990). Chronology of expansion and contraction of four Great Basin lake systems during the past 35,000 years. *Palaeogeography, Palaeoclimatology, Palaeoecology*, *78*(3–4), 241–286. https://doi.org/10.1016/0031-0182(90)90217-U

Bunds, M. P., Scott, C. P., Whitney, B., & Lee, V. J. C. (2021). *High resolution topography of the Southern San Andreas fault from Painted Canyon to Bombay Beach, USA* [Dataset]. Distributed by OpenTopography. https://doi.org/10.5069/G94M92RG

Crone, A. J., Machette, M. N., Bonilla, M. G., Lienkaemper, J. J., Pierce, K. L., Scott, W. E., & Bucknam, R. C. (1987). Surface faulting accompanying the Borah Peak earthquake and segmentation of the lost river fault, central Idaho. *Bulletin of the Seismological Society of America*, *77*(3), 739–770. https://doi.org/10.1785/BSSA0770030739

Delong, S. (2017). *Classified point cloud data from the 2005 B4 Lidar Project, southern California* [Dataset]. U.S. Geological Survey. https://doi.org/10.5066/F7TQ5ZQ6

DuRoss, C. B., Gold, R. D., Dawson, T. E., Scharer, K. M., Kendrick, K. J., Akciz, S. O., Angster, S. J., Bachhuber, J., Bacon, S., Bennett, S. E. K., Blair, L., Brooks, B. A., Bullard, T., Burgess, W. P., Chupik, C., DeFrisco, M., Delano, J., Dolan, J. F., Frost, E., … Zinke, R. (2020). Surface displacement distributions for the July 2019 Ridgecrest, California, earthquake ruptures. *Bulletin of the Seismological Society of America*, *110*(4), 1400–1418. https://doi.org/10.1785/0120200058

Earth Resources Observation and Science (EROS) Center. (2017). *National Aerial Photography Program 1:40,000 Scale* [Tiff]. U.S. Geological Survey. https://doi.org/10.5066/F7VD6WQZ

Farr, T. G., & Kobrick, M. (2000). Shuttle radar topography mission produces a wealth of data. *Eos, Transactions American Geophysical Union*, *81*(48), 583. https://doi.org/10.1029/EO081i048p00583

Graymer, R. W., Brabb, E. E., Jones, D. L., Barnes, J., Nicholson, R. S., & Stamski, R. E. (2007). *Geologic map and map database of eastern Sonoma and western Napa Counties, California* [Map]. http://pubs.usgs.gov/sim/2007/2956/

Machette, M. N., Personius, S. F., Nelson, A. R., Schwartz, D. P., & Lund, W. R. (1991). The Wasatch fault zone, Utah—Segmentation and history of Holocene earthquakes. *Journal of Structural Geology*, *13*(2), 137–149. https://doi.org/10.1016/0191-8141(91)90062-N

Manighetti, I., Perrin, C., Dominguez, S., Garambois, S., Gaudemer, Y., Malavieille, J., Matteo, L., Delor, E., Vitard, C., & Beauprêtre, S. (2015). Recovering paleoearthquake slip record in a highly dynamic alluvial and tectonic region (Hope Fault, New Zealand) from airborne lidar. *Journal of Geophysical Research: Solid Earth*, *120*(6), 4484–4509. https://doi.org/10.1002/2014JB011787

Mapel, W. J., Read, W. H., & Smith, R. K. (1965). *Geologic map and sections of the Doublespring quadrangle, Custer and Lemhi Counties, Idaho* (GQ-464) [Map]. https://doi.org/10.3133/gq464

Mueller, K. J., & Rockwell, T. K. (1991). Late Quaternary structural evolution of the western margin of the Sierra Cucapa, Northern Baja California. In J. P. Dauphin & B. R. T. Simoneit, *The Gulf and Peninsular Province of the Californias*. American Association of Petroleum Geologists. https://doi.org/10.1306/M47542C14

Mueller, K. J., & Rockwell, T. K. (1995). Late Quaternary activity of the Laguna Salada fault in northern Baja California, Mexico. *Geological Society of America Bulletin*, *107*(1), 8. https://doi.org/10.1130/0016-7606(1995)107<0008:LQAOTL>2.3.CO;2

Nissen, E., Maruyama, T., Ramon Arrowsmith, J., Elliott, J. R., Krishnan, A. K., Oskin, M. E., & Saripalli, S. (2014). Coseismic fault zone deformation revealed with differential lidar: Examples from Japanese M w ∼7 intraplate earthquakes. *Earth and Planetary Science Letters*, *405*, 244–256. https://doi.org/10.1016/j.epsl.2014.08.031

OpenTopography. (2010). *Napa Watershed, CA* [Dataset]. Distributed by OpenTopography. https://doi.org/10.5069/G9BG2KW9. Accessed 1 Jul 2024.

OpenTopography. (2012). *2006 INEGI Sierra Cucupah Empirically Corrected Lidar Dataset* [Dataset]. Distributed by OpenTopography. https://doi.org/10.5069/G9S180F8. Accessed 1 Jul 2024

OpenTopography. (2014). *State of Utah Acquired LiDAR Data—Wasatch Front* [Dataset]. Distributed by OpenTopography. https://doi.org/10.5069/G9TH8JNQ. Accessed 28 Jun 2024.

OpenTopography. (2016). *Marlborough Fault System, South Island, New Zealand* [Dataset]. Distributed by OpenTopography. https://doi.org/10.5069/G9G44N75. Accessed 28 Jun 2024.

OpenTopography. (2019). *2019 Ridgecrest, CA Pre-Earthquake Digital Surface Model* [Dataset]. Distributed by OpenTopography. https://doi.org/10.5069/G998854C. Accessed 3 Jul 2024.

Peel, M. C., Finlayson, B. L., & McMahon, T. A. (2007). Updated world map of the Köppen-Geiger climate classification. *Hydrology and Earth System Sciences*, *11*(5), 1633–1644. https://doi.org/10.5194/hess-11-1633-2007

Philibosian, B. E., Jobe, J. A., Chupik, C., Dawson, T., Bennett, S., Kendrick, K. J., Duross, C. B., Gold, R. D., Ladinsky, T., Haddon, E. K., Pierce, I., Swanson, B., & Seitz, G. (2020). *Pre-existing features associated with active faulting in the vicinity of the 2019 Ridgecrest, California earthquake sequence* [Dataset]. U.S. Geological Survey. https://doi.org/10.5066/P9ENA24Y

Ponti, D. J., Pickering, A. J., Blair, J. L., Rosa, C. M., Thomas, K., & Dawson, T. (2020). *Digital datasets documenting surface fault rupture and ground deformation features produced by the Ridgecrest M6.4 and M7.1 earthquake sequence of July 4 and 5, 2019* [Dataset]. U.S. Geological Survey. https://doi.org/10.5066/P9BZ5IJ9

Sarmiento, A., Madugo, D., Bozorgnia, Y., Shen, A., Mazzoni, S., Lavrentiadis, G., Dawson, T., Madugo, C., Kottke, A., Thompson, S., Baize, S., Milliner, C., Nurminen, F., Boncio, P., & Visini, F. (2021). *Fault Displacement Hazard Initiative Database* (GIRS-2021-08). UCLA Natural Hazards Risk And Resiliency Research Center. https://www.risksciences.ucla.edu/girs-reports/2021/08

Thompson Jobe, J. A., Philibosian, B., Chupik, C., Dawson, T., K. Bennett, S. E., Gold, R., DuRoss, C., Ladinsky, T., Kendrick, K., Haddon, E., Pierce, I., Swanson, B., & Seitz, G. (2020). Evidence of previous faulting along the 2019 Ridgecrest, California, earthquake ruptures. *Bulletin of the Seismological Society of America*, *110*(4), 1427–1456. https://doi.org/10.1785/0120200041

Toda, S., & Tsutsumi, H. (2013). Simultaneous reactivation of two, subparallel, inland normal faults during the Mw 6.6 11 April 2011 Iwaki earthquake triggered by the Mw 9.0 Tohoku-oki, Japan, earthquake. *Bulletin of the Seismological Society of America*, *103*(2B), 1584–1602. https://doi.org/10.1785/0120120281